

EARTH SCIENCES

Olivine-norite rock detected by the lunar rover Yutu-2 likely crystallized from the SPA-impact melt pool

Honglei Lin^{1,†}, Zhiping He^{2,†}, Wei Yang¹, Yangting Lin^{1,*}, Rui Xu², Chi Zhang¹, Meng-Hua Zhu³, Rui Chang¹, Jinhai Zhang¹, Chunlai Li², Hongyu Lin⁴, Yang Liu⁵, Sheng Gou⁶, Yong Wei¹, Sen Hu¹, Changbin Xue⁷, Jianfeng Yang⁸, Jie Zhong⁹, Xiaohui Fu¹⁰, Weixing Wan¹ and Yongliao Zou⁵

ABSTRACT

Chang'E-4 landed in the South Pole-Aitken (SPA) basin, providing a unique chance to probe the composition of the lunar interior. Its landing site is located on ejecta strips in Von Kármán crater that possibly originate from the neighboring Finsen crater. A surface rock and the lunar regolith at 10 sites along the rover Yutu-2 track were measured by the onboard Visible and Near-Infrared Imaging Spectrometer in the first three lunar days of mission operations. *In situ* spectra of the regolith have peak band positions at 1 and 2 μm , similar to the spectral data of Finsen ejecta from the Moon Mineralogy Mapper, which confirms that the regolith's composition of the landing area is mostly similar to that of Finsen ejecta. The rock spectrum shows similar band peak positions, but stronger absorptions, suggesting relatively fresh exposure. The rock may consist of $38.1 \pm 5.4\%$ low-Ca pyroxene, $13.9 \pm 5.1\%$ olivine and $48.0 \pm 3.1\%$ plagioclase, referred to as olivine-norite. The plagioclase-abundant and olivine-poor modal composition of the rock is inconsistent with the origin of the mantle, but representative of the lunar lower crust. Alternatively, the rock crystallized from the impact-derived melt pool formed by the SPA-impact event via mixing the lunar crust and mantle materials. This scenario is consistent with fast-cooling thermal conditions of a shallow melt pool, indicated by the fine to medium-sized texture (<3 mm) of the rock and the SPA-impact melting model [*Icarus* 2012; 220: 730–43].

Keywords: impact basin, lunar interior composition, visible and near-infrared spectra, lunar rover Yutu-2, Chang'E-4 mission

INTRODUCTION

According to the Lunar Magma Ocean (LMO) hypothesis [1–3], the Moon was, early in its history, covered by global silicate magma up to 800 km thick [4], which crystallized into the modern crust and mantle. Several model compositions of the lunar mantle and crust have been proposed, with the low-ermost cumulates dominated by Mg-rich olivine, followed by orthopyroxene (OPX) and finally by Ca pyroxene and plagioclase [5,6]. Furthermore, the lunar-mantle composition may have been modified by the overturn process, with the heavy top mantle materials sinking down due to gravitational instability [7]. In order to constrain the Moon's formation history, it is critically important to determine the

composition of the lunar deep interior. The South Pole-Aitken (SPA) basin is the largest impact basin on the Moon, 2200 km in mean diameter and 13 km in depth [8,9], theoretically opening a window into the lunar lower crust and likely into the upper mantle [10–12]. However, compositional information of the SPA basin has mainly been obtained from orbital remote sensing [13–15] and there have been no *in situ* measurements of the region before the first landing on the far side of the Moon by Chang'E-4.

On 3 January 2019, the Chinese lunar mission Chang'E-4 (CE-4), the backup of Chang'E-3 (CE-3), landed at 45.457°S , 177.588°E in Von Kármán crater (Fig. 1A), which is within the Mg-Pyroxene Annulus [13] of the SPA basin. Von

¹Key Laboratory of Earth and Planetary Physics, Institute of Geology and Geophysics, Chinese Academy of Sciences, Beijing 100029, China; ²Key Laboratory of Space Active Opto-Electronics Technology, Shanghai Institute of Technical Physics, Chinese Academy of Sciences, Shanghai 200083, China; ³State Key Laboratory of Lunar and Planetary Sciences, Macau University of Science and Technology, Macau, China; ⁴Beijing Institute of Space Mechanics and Electricity, Beijing 100076, China; ⁵State Key Laboratory of Space Weather, National Space Science Center, Chinese Academy of Sciences, Beijing 100190, China; ⁶State Key Laboratory of Remote Sensing Science, Institute of Remote Sensing and Digital Earth, Chinese Academy of Sciences, Beijing 100101, China; ⁷Key Laboratory of Electronics and Information Technology for Space System, National Space Science Center, Chinese Academy of Sciences, Beijing 100190, China; ⁸Xi'an Institute of Optics and Precision Mechanics, Chinese Academy of Sciences, Xi'an 710119, China; ⁹Institute of Optics and Electronics, Chinese Academy of Sciences, Chengdu 610209, China and ¹⁰Shandong Provincial Key Laboratory of Optical Astronomy and Solar-Terrestrial Environment, Institute of Space Sciences, Shandong University, Weihai 264209, China

* Corresponding author.

E-mail:

linyt@mail.iggcas.ac.cn

[†] Equally contributed to this work.

Received 6 July 2019;

Revised 11 October 2019;

Accepted 9 November 2019

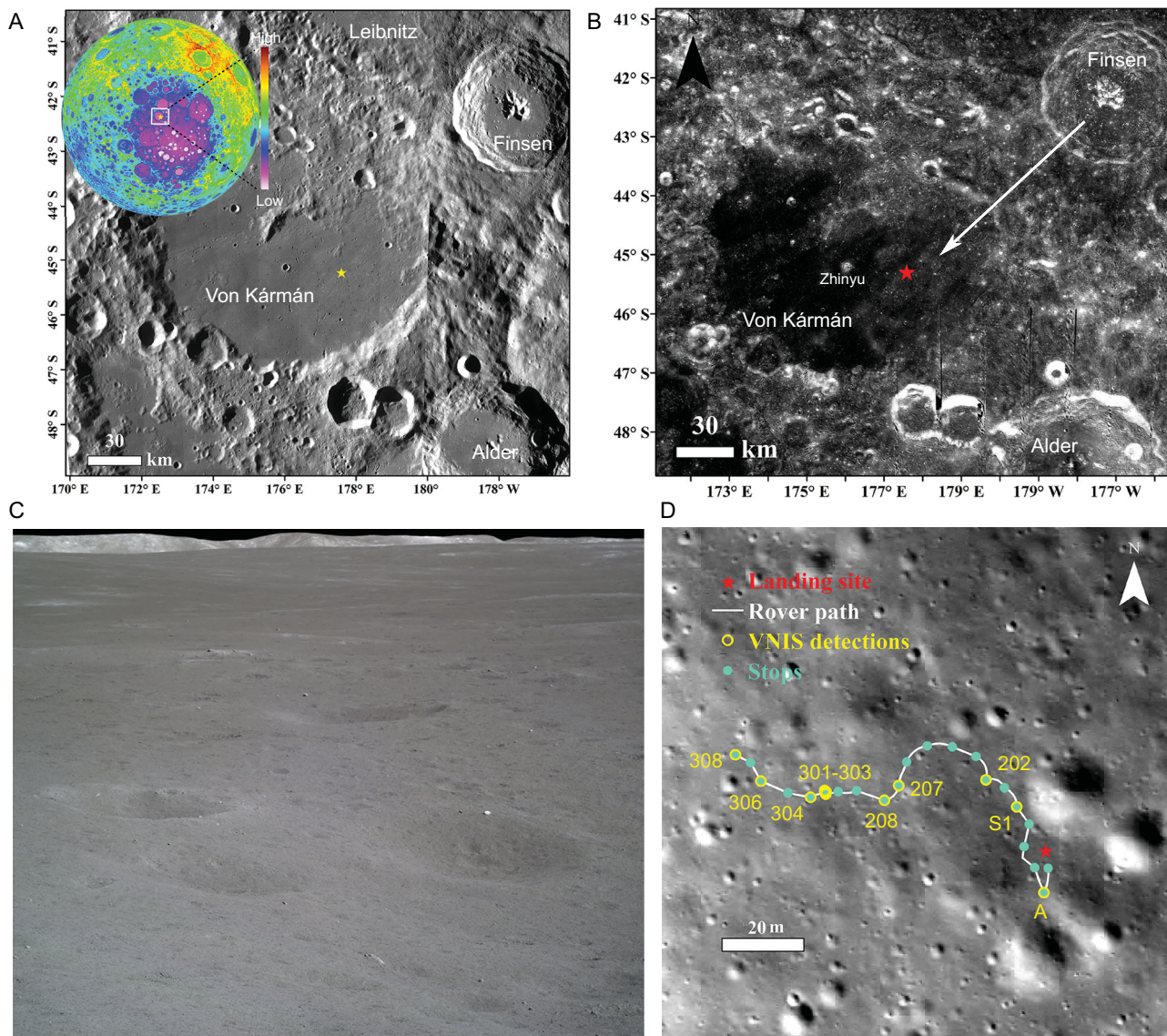


Figure 1. CE-4 landing site and the rover track. (A) The geologic setting of the CE-4 landing site (yellow star) seen in a Lunar Reconnaissance Orbiter Camera (LROC) Wide Angle Camera (WAC) image. The inset is SLDEM (SELENE and LRO DEM 2015) [16], stretched from -8000 to $10\,000$ m. (B) The ejecta strips radiating from Finsen crater. Zhinyu crater, the largest crater close to the landing site, is also labeled. (C) The typical landscape of the CE-4 landing site, showing very few rocks overlying the lunar regolith. (D) The Yutu-2 rover traverse during the first 3 lunar days of mission operations. The context image was taken by the descent camera on CE-4. The red star is the location of CE-4 landing site and the scale bar is 20 m.

Kármán crater has been filled with mare basalt and partially covered by ejecta from nearby impact craters. The landing site is located on ejecta strips radiating from Finsen crater, which lies ~ 135 km to the northeast (Fig. 1B). The lunar surface at the landing site consists of very homogenous regolith overlain by a few scattered rocks (Fig. 1C). During the first three lunar days of mission operations, the Visible and Near-Infrared Imaging Spectrometer (VNIS) on board the rover Yutu-2 measured nine hyperspectral images of the lunar regolith and one hyperspectral image of a rock boulder along the 163-m rover track (Fig. 1D). These *in situ* measurements of the lunar regolith

and overlying rock reveal the fine-scale composition of the SPA basin at unprecedented spatial resolution, shedding light on the composition of the lunar interior and the LMO crystallization.

RESULTS

The radiance spectra measured by VNIS on board Yutu-2 were converted to reflectance via division of the solar irradiance spectrum and then were photometrically corrected using an empirical photometric function (see ‘Materials and methods’). The spectra were smoothed twice with a boxcar average of 17 pixels followed by another boxcar average of

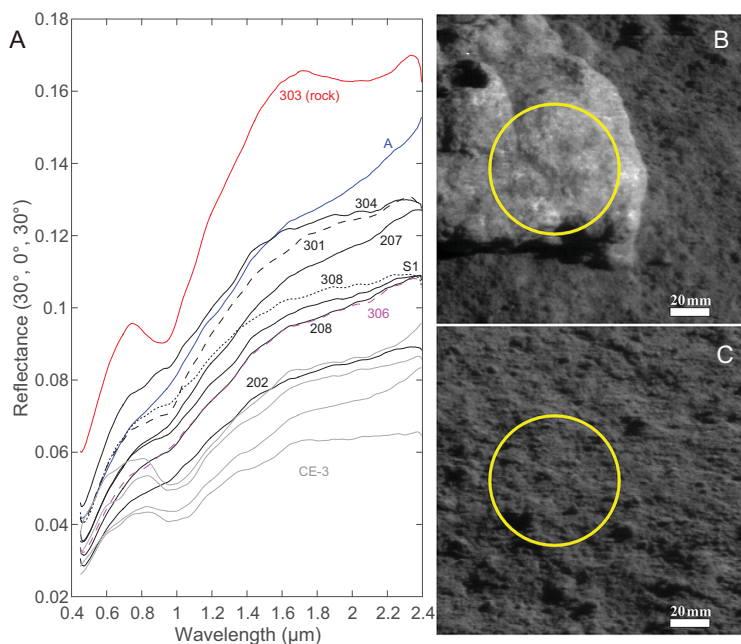


Figure 2. (A) VNIS spectra of the rock and lunar regolith measured by Chang'E-4. The analysis labels are the same as in Fig. 1D. Four other spectra (in gray color) of the basaltic lunar regolith measured by Chang'E-3 [17] are shown for comparison. (B) and (C) are the CMOS images of the rock (labeled as 303) and the lunar soil (labeled as 207) at $0.75 \mu\text{m}$ observed by VNIS imaging spectrometer, respectively. The yellow circle is the SWIR field and the scale bar is 20 mm.

7 pixels. All 10 VNIS spectra, including 1 of the rock boulder and 9 of the lunar regolith, are shown in Fig. 2 alongside a close-up image of the rock and an image of the lunar regolith. The other images of the regolith are given in the Supplementary Materials (Supplementary Fig. 5). The surface around the CE-4 landing site is distinctly brighter than the basaltic soils at the Chang'E-3 landing site, which is exhibited by their different albedos (Fig. 2A).

The spectra of the lunar regolith and the rock show maximum absorptions at ~ 1 and $\sim 2 \mu\text{m}$ (Fig. 2A and Supplementary Fig. 10). The peak positions of the ~ 1 - and ~ 2 - μm bands can be used to distinguish low-calcium pyroxene (LCP, centered at ~ 0.95 and $\sim 1.9 \mu\text{m}$) from high-calcium pyroxene (HCP, centered at ~ 1.0 and $\sim 2.0 \mu\text{m}$) [18] and to detect the possible presence of olivine (centered at $\sim 1.1 \mu\text{m}$). The precise peak positions were determined by searching for the minimum reflectance [19] of the bands in continuum-removed [20] spectra (see 'Materials and methods'). As shown in Fig. 3, the pyroxene composition of the lunar-surface materials measured by Yutu-2 is close to LCP, which is obviously different with the basalts excavated from Zhinyu crater.

The abundances of the constituents (i.e. agglutinates, total pyroxene, augite, olivine and plagioclase) of lunar regolith show strong correlation with

the spectral parameters (empirical combination of albedos in the principal spectral bands) [25,26]. As such, we used a Lunar Soil Characterization Consortium (LSCC) dataset [27] to estimate the modal compositions of the regolith at the ChangE-4 landing site (see 'Materials and methods' and Supplementary Materials). The estimated results are summarized in Table 1, with an average modal composition of $55.9 \pm 0.7\%$ agglutinates (AGG), $13.5 \pm 0.9\%$ pyroxene (PYX) ($4.9 \pm 0.5\%$ HCP, $8.6 \pm 0.4\%$ LCP), $13.6 \pm 0.7\%$ plagioclase (PLG) and $1.4 \pm 0.3\%$ olivine (OL). The maturity parameter I_s/FeO can be derived from VNIS reflectance (Ref) spectra using equation S5 ($0.0341 \times \text{Ref}_{500 \text{ nm}} - 0.2421 \times \text{Ref}_{750 \text{ nm}} - 0.0201 \times \text{Ref}_{900 \text{ nm}} + 0.2074 \times \text{Ref}_{1000 \text{ nm}} + 1.9430$) [25,28] (see Supplementary Materials). The results are listed in Table 1.

The rock analysed by Yutu-2 is >20 cm in size, sitting on the regolith surface. No grains can be unambiguously recognized on the surface, suggesting a fine- or medium-grain-size texture (<3 mm) based on the 0.6-mm/pixel spatial resolution of the image (Fig. 2B). In addition, the rock shows no lithic clasts of lunar-impact breccia (Supplementary Fig. 15), which usually vary in brightness and are embedded in a dark fine-grained matrix. The rock shows deep absorptions at ~ 1 - and ~ 2 - μm bands due to the low degree of space weathering. Hapke radiative transfer modeling [29], which has been validated and applied to lunar samples and meteorites [30,31] (see Supplementary Materials), was used to estimate the modal composition of the rock and our modeling results suggest $38.1 \pm 5.4\%$ LCP, $13.9 \pm 5.1\%$ olivine and $48.0 \pm 3.1\%$ plagioclase in this rock sample. As such, it is referred to as olivine-norite.

DISCUSSION AND CONCLUSION

The spectral features at site A are distinct from those at other sites (Fig. 2A), resulting in different estimated modal mineral compositions and maturity (Table 1). Site A shows the highest agglutinates and I_s/FeO value, indicating greater maturity than the other sites. Comparison to images acquired by the Lunar Reconnaissance Orbiter (LRO) Narrow Angle Camera (NAC) shows that the surface disturbed by CE-4 descent engines is about 1400 m^2 (Supplementary Fig. 3), which is in agreement with the relationship between lander mass and blast-zone area constrained by previous missions [32]. Site A, about 11.5 m from the lander, should have been most significantly affected by the rocket exhaust. The higher maturity value at site A is therefore probably caused by deposition of the finest dust particles that were transported from the topmost surface below the lander blown by the rocket exhaust [33].

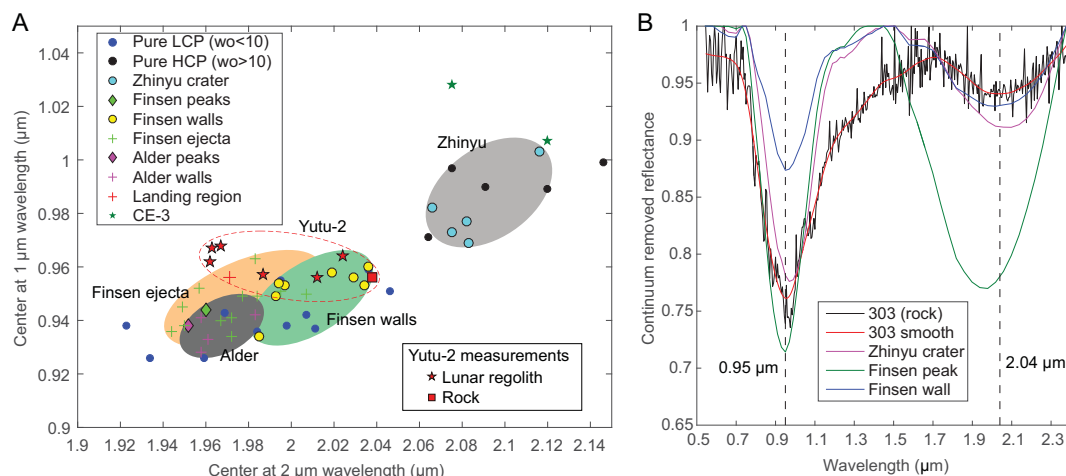


Figure 3. Spectral features of the lunar-surface materials observed by Yutu-2. (A) The peak center positions of the 1- and 2- μm bands, which are compared with those from spectra measured by CE-3 and the Moon Mineralogy Mapper (M^3) of nearby craters. The pure LCP and HCP data are from [21]. The locations of all the M^3 spectra are labeled in Supplementary Fig. 14. (B) Comparison of the rock spectrum with spectra from Zhinyu crater, Alder crater peak, Finsen crater peak and Finsen crater wall. The spectral calibration error of VNIS onboard CE-3 and CE-4 is $<2\text{ nm}$ [22,23] and that of M^3 is $<1\text{ nm}$ [24].

Table 1. The estimated modal compositions and I_s/FeO values of the lunar regolith measured by the Yutu-2 rover^a.

| Site | AGG | PYX | HCP | PLG | OL | I_s/FeO | D (m) |
|-------------|-------------|-------------|-------------|-------------|-------------|------------------|---------|
| Uncertainty | $\pm 7.7\%$ | $\pm 3.1\%$ | $\pm 1.3\%$ | $\pm 4.4\%$ | $\pm 0.8\%$ | ± 18.8 | – |
| A | 57.1 | 11.5 | 3.8 | 15.0 | 1.6 | 97.0 | 11.5 |
| S1 | 55.6 | 14.2 | 5.2 | 13.0 | 1.5 | 78.7 | 20.1 |
| 202 | 55.6 | 14.4 | 5.3 | 13.6 | 1.7 | 85.1 | 29.4 |
| 207 | 56.7 | 12.9 | 4.4 | 14.1 | 1.7 | 89.2 | 51.3 |
| 208 | 56.3 | 13.9 | 5.2 | 12.9 | 1.7 | 86.0 | 54.5 |
| 301 | 55.2 | 13.6 | 4.8 | 14.1 | 1.3 | 76.6 | 71.3 |
| 304 | 55.4 | 13.1 | 4.9 | 13.6 | 0.9 | 76.3 | 68.9 |
| 306 | 56.1 | 13.6 | 4.9 | 13.4 | 1.4 | 86.8 | 85.8 |
| 308 | 55.2 | 14.2 | 5.5 | 12.9 | 1.1 | 74.0 | 98.1 |

^aAGG, agglutinates; PYX, pyroxene; HCP, augite; PLG, plagioclase; OL, olivine. D is the straight-line distance from the analysis position to the lander.

The regolith at the CE-4 landing site is dominated by plagioclase and pyroxenes with more LCP than HCP (1.8:1) (Table 1), consistently with the findings of a recent study [34]. The estimated modal composition of the lunar regolith is inconsistent with mare basalts (which would contain more pyroxene than plagioclase, with higher HCP than LCP) [35], but suggests its main source was norite [36]. Figure 3 also shows that band positions from *in situ* spectra of the lunar regolith at the landing site fall within the ranges of Finsen crater materials (the ejecta and crater walls), which are distinct from the underlying mare basalt excavated by Zhinyu crater (Supplementary Fig. 13) and the basaltic regolith on the nearside of the Moon that was analysed by Yutu-1 [17].

Our observations are also supported by topographic features. The landing site is located on NE–SW ejecta strips radiating from Finsen crater (Fig. 4), which superpose the SE–NW dome-like

ridge directed towards Alder crater (Fig. 4A). Furthermore, the elevation difference between the landing site and the edge of the SE–NW dome-like ridge was estimated to be $\sim 70\text{ m}$, suggesting a very thick deposit of ejecta from Finsen crater and probably also from Alder crater. Previous studies also reported that mare basalts were deeply buried by ejecta from nearby craters, with a minimum burial depth of 33 m [37,38]. Hence, the surface materials at the landing site are predominantly ejecta from neighboring craters, with little contribution from the underlying mare basalt.

The rock analysed by Yutu-2 is olivine-norite, not basalt. This is consistent with its setting on the surface of the regolith. Its modal composition is close to that of the regolith, but has higher modal abundances of olivine and LCP. It is possible that the rock was also delivered to its current location from Finsen crater. This is consistent with the similar peak

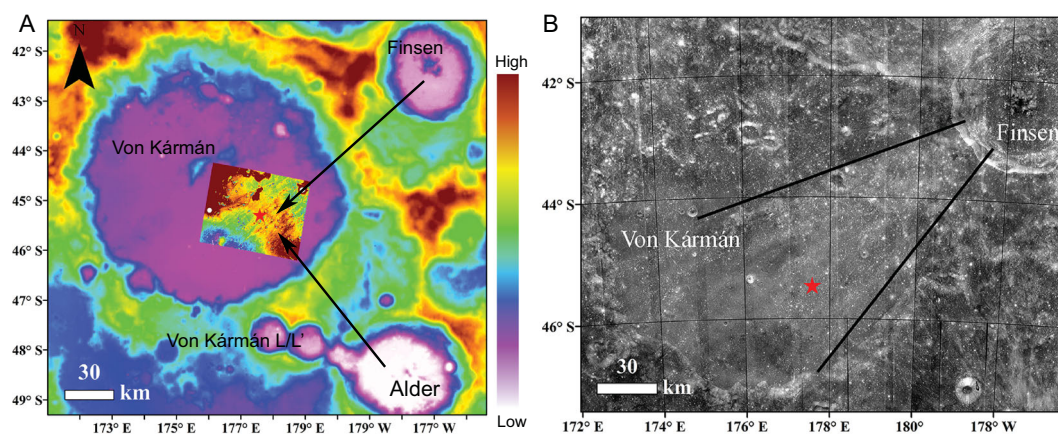


Figure 4. (A) SLDEM [16]. The image is stretched from -7581 to -158 m. The inset image is stretched from -6000 to -5900 m. (B) MI band ratio of 415 and 750 nm [39] (stretched from 0.53 to 0.55). The landing site is marked as a red star.

positions of 1- and 2- μm bands (Fig. 3A). Alternatively, this rock may have been excavated from Alder crater. In this case, it would have been covered by ejecta from Finsen crater and then subsequently excavated from depth. However, this uncertainty makes no difference for constraining the composition of SPA basin, because both Finsen and Alder craters are located within the Mg-Pyroxene Annulus [13] at a similar distance (~ 350 km) from the center of SPA basin. Hence, this rock is likely representative of the original bedrock in the Mg-Pyroxene Annulus of SPA basin.

The SPA-impact event excavated the lunar deep interior and exposed lunar lower crust and/or mantle materials [10,12]. The bedrock of SPA basin could be the original plutonic rocks crystallized directly from LMO or may have formed from crystallization of the SPA-impact melt pool. The plagioclase-abundant and olivine-poor modal compositions of the materials measured by Yutu-2 rover are consistent with the origin of the lower crust rather than the mantle. The deep interior origin would also expect coarse-grained textures, typical of plutonic rocks (3 mm or larger) [40,41]. However, the observed fine- to medium-grain-sized texture of the rock suggests a fast-cooling thermal condition, which is consistent with crystallization from the SPA-impact melt pool [10,15,42]. Furthermore, the numerical simulations of impacting suggest that the SPA-scale event could generate a transient cavity with a diameter of 840 km and a melt pond with ~ 50 -km depth (Fig. 5A) [10,42,43]. The SPA-impact melt would have been a mixture of the lunar crust and upper-mantle materials. Both Finsen and Alder craters are located close to the margin of the melt pond (Fig. 5) [9,10]. Hence, the sources of the regolith and the rock boulder analysed by Yutu-2 are unlikely to be representative of the original lunar lower crust or the mantle as

claimed by the previous study [44], but rather are the differentiated rocks from the impact melt pond. It is likely that the Finsen-impact event excavated shallow-layer materials crystallized from the SPA melt pond and delivered them to Von Kármán crater, where they were measured by the rover Yutu-2 (Fig. 5).

In summary, the *in situ* spectral measurements of the rock and regolith at the Chang'E-4 landing site result in similar estimates for mineral compositions and the rock is likely olivine-norite. These surface materials were delivered mainly from the neighboring Finsen crater, with possible additional contributions from Alder crater, but not from the underlying mare basalts. The fine- to medium-grain-size texture of the rock suggests fast crystallization, probably from the impact melt pond produced via melting the lunar lower crust and mantle materials by the SPA basin-forming event. This scenario is also consistent with the SPA-impact melting models [10]. These observations shed light on the composition of the SPA basin floor and the formation of the SPA basin.

MATERIALS AND METHODS

Data preprocessing

The VNIS on board the rover Yutu-2 consists of a Complementary Metal-Oxide Semiconductor (CMOS) imager (450–950 nm) with 256×256 pixels and a short-wavelength near-infrared (SWIR) detector (950–2395 nm) with single-pixel [22,45]. VNIS is installed on the front of the rover and measures the lunar surface from a height of ~ 1 m above the lunar surface at a 45° emission angle. The SWIR field is centered at pixel 97.5, 127.5 of the CMOS field with a diameter of 107.6 pixels (Supplementary Fig. 1). The spectral-sampling interval of the CMOS and SWIR detectors is 5 nm, and the wavelength and

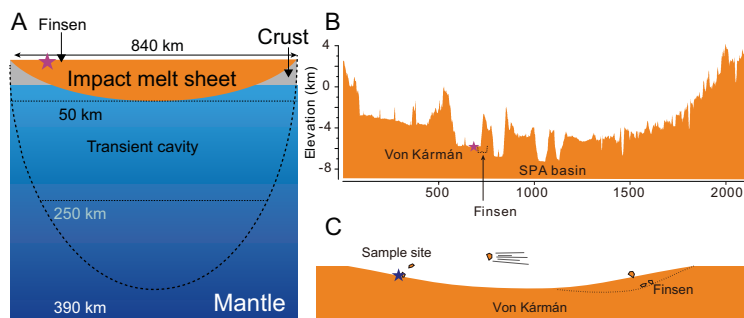


Figure 5. Schematic illustration for the origin of the rock and regolith analysed by Yutu-2. (A) The impact event of SPA formed a transient crater that was ~ 840 km in diameter and ~ 390 km in depth [10,43]. Hydrocode models suggest that the upper ~ 250 km of the lunar interior was melted [43] and the melts gathered at the bottom of the SPA basin to form a ~ 50 -km-deep melt pond after impact [10,43]. (B) The topographic profile from A to A' shown in Supplementary Fig. 2. (C) The schematic illustration of the sputtering process of the rock.

FWHM (full width at half maximum) are shown in Supplementary Table 6.

The data were calibrated in flight and converted to reflectance using solar irradiance [46] and were then photometrically corrected [47,48] to common viewing geometry (incidence angle = 30° , emission angle = 0° and phase angle = 30°) based on illumination simulations conducted with lunar regolith simulants [49] (Supplementary Fig. 7). The detailed description of this process is available in the Supplementary Materials.

The continuum is derived by fitting a convex hull over the top of a spectrum using straight-line segments (Supplementary Fig. 9) that connect local spectra maxima [20]. The band center position is defined as the minimum of a third-order polynomial fit to the channels of the band minimum [19]. All the Moon Mineralogy Mapper (M^3) spectra and laboratory spectra used in this study were resampled to VNIS bands with a Gaussian model and the continuum-removed spectra were derived using the spectral range of $0.545\text{--}2.395\ \mu\text{m}$.

Estimation of the mineral abundances from the regolith spectra

The statistical formulations linking spectral properties (empirical combination of spectral bands) with each mineral abundance were optimized with LSCC soils and have been successfully applied to Clementine UVVIS data [25,26]. We resampled the LSCC spectra to the spectral resolutions of Yutu-2 VNIS bands using a Gaussian model and parameterized the formulations (Supplementary Table 4) to estimate the mineralogy and maturity parameter of the regolith at the CE-4 landing site. The detailed

descriptions are available in the Supplementary Materials.

Estimation of the mineral abundance from the rock spectrum

The rock is much less affected by space weathering than the soil and has typical spectral characteristics. Thus, a more rigorous non-linear model, i.e. a Hapke radiative transfer model [29], was applied to retrieve the mineral abundances of the rock. The endmembers used in this study are high-calcium pyroxene (HCP), low-calcium pyroxene (LCP), olivine (OL) and plagioclase (PLG) (Supplementary Fig. 11 and Supplementary Table 5). More details about the methods are available in Supplementary Materials.

SUPPLEMENTARY DATA

Supplementary data are available at *NSR* online.

DATA AVAILABILITY

The data reported in this work will be archived at http://moon.bao.ac.cn/searchOrder_dataSearchData.search.

ACKNOWLEDGEMENTS

The Chang'E-4 mission was carried out by the Chinese Lunar Exploration Program and the data were provided by the Science and Application Center for Moon and Deep Space Exploration, Chinese Academy of Sciences. The authors are grateful to the editor and three anonymous reviewers for their constructive reviews.

FUNDING

This work was supported by the Key Research Program of Frontier Sciences, Chinese Academy of Sciences (QYZDJ-SSW-DQC001), the National Natural Science Foundation of China (41902318, 41490631, 41525016, 11941001) and the Beijing Municipal Science and Technology Commission (Z181100002918003).

AUTHOR CONTRIBUTIONS

L.Y.T., Y.W. and L.H.L. designed the research; L.H.L., Y.W. and L.Y.T. performed research; H.Z.P., X.R., L.C.L., L.H.Y., Y.J.F., Z.J. and X.C.B. contributed new reagents/analytic tools; L.H.L., H.Z.P., X.R., L.Y.T., Z.C., Z.J.H., H.S. and C.R. analysed data; L.Y.T., L.H.L., W.Y., Z.M.H., W.W.X., Z.Y.L., L.Y., F.X.H. and G.S. wrote the paper.

Conflict of interest statement. None declared.

REFERENCES

- Warren PH. The Magma Ocean concept and lunar evolution. *Annu Rev Earth Planet Sci* 1985; **13**: 201–40.

2. Wood JA, Dickey JS Jr and Marvin UB *et al.* Lunar anorthosites and a geophysical model of the moon. *Geochim Cosmochim Acta* 1970; **1**: 965–88.
3. Smith J, Anderson A and Newton R *et al.* Petrologic history of the moon inferred from petrography, mineralogy and petrogenesis of Apollo 11 rocks. *Geochim Cosmochim Acta* 1970; **1**: 897–925.
4. Elkins-Tanton LT, Burgess S and Yin Q-Z. The lunar magma ocean: reconciling the solidification process with lunar petrology and geochronology. *Earth Planet Sci Lett* 2011; **304**: 326–36.
5. Rapp J and Draper D. Fractional crystallization of the lunar magma ocean: updating the dominant paradigm. *Meteorit Planet Sci* 2018; **53**: 1432–55.
6. Lin YH, Tronche EJ and Steenstra ES *et al.* Evidence for an early wet moon from experimental crystallization of the lunar magma ocean. *Nat Geosci* 2017; **10**: 14–8.
7. Hess PC and Parmentier E. A model for the thermal and chemical evolution of the Moon's interior: implications for the onset of mare volcanism. *Earth Planet Sci Lett* 1995; **134**: 501–14.
8. Smith DE, Zuber MT and Neumann GA *et al.* Initial observations from the lunar orbiter laser altimeter (LOLA). *Geophys Res Lett* 2010; **37**: L18204.
9. Garrick-Bethell I and Zuber MT. Elliptical structure of the lunar South Pole-Aitken basin. *Icarus* 2009; **204**: 399–408.
10. Potter RWK, Collins GS and Kiefer WS *et al.* Constraining the size of the South Pole-Aitken basin impact. *Icarus* 2012; **220**: 730–43.
11. James PB, Smith DE and Byrne PK *et al.* Deep structure of the lunar South Pole-Aitken basin. *Geophys Res Lett* 2019; **49**: 5100–6.
12. Melosh H, Kendall J and Horgan B *et al.* South Pole-Aitken basin ejecta reveal the Moon's upper mantle. *Geology* 2017; **45**: 1063–6.
13. Moriarty DP and Pieters CM. The character of South Pole-Aitken basin: patterns of surface and subsurface composition. *J Geophys Res Planets* 2018; **123**: 729–47.
14. Ohtake M, Uemoto K and Yokota Y *et al.* Geologic structure generated by large-impact basin formation observed at the South Pole-Aitken basin on the moon. *Geophys Res Lett* 2014; **41**: 2738–45.
15. Uemoto K, Ohtake M and Haruyama J *et al.* Evidence of impact melt sheet differentiation of the lunar South Pole-Aitken basin. *J Geophys Res Planets* 2017; **122**: 1672–86.
16. Barker MK, Mazarico E and Neumann GA *et al.* A new lunar digital elevation model from the lunar orbiter laser altimeter and SELENE terrain camera. *Icarus* 2016; **273**: 346–55.
17. Zhang JH, Yang W and Hu S *et al.* Volcanic history of the Imbrium basin: a close-up view from the lunar rover Yutu. *Proc Natl Acad Sci USA* 2015; **112**: 5342–7.
18. Adams JB. Visible and near-infrared diffuse reflectance spectra of pyroxenes as applied to remote sensing of solid objects in the solar system. *J Geophys Res* 1974; **79**: 4829–36.
19. Horgan BHN, Cloutis EA and Mann P *et al.* Near-infrared spectra of ferrous mineral mixtures and methods for their identification in planetary surface spectra. *Icarus* 2014; **234**: 132–54.
20. Clark RN. Water frost and ice: The near-infrared spectral reflectance 0.65–2.5 μm . *J Geophys Res Solid Earth* 1981; **86**: 3087–96.
21. Klima RL, Pieters CM and Dyar MD. Spectroscopy of synthetic mg-Fe pyroxenes I: spin-allowed and spin-forbidden crystal field bands in the visible and near-infrared. *Meteorit Planet Sci* 2007; **42**: 235–53.
22. He ZP, Wang BY and Lu G *et al.* Operating principles and detection characteristics of the visible and near-infrared imaging spectrometer in the Chang'e-3. *Res Astron Astrophys* 2014; **14**: 1567–77.
23. Li CL, Wang ZD and Xu R *et al.* The scientific information model of Chang'e-4 visible and near-IR imaging spectrometer (VNIS) and in-flight verification. *Sensors* 2019; **19**: 2806.
24. Green RO, Pieters C and Mouroulis P *et al.* The Moon Mineralogy Mapper (M³) imaging spectrometer for lunar science: Instrument description, calibration, on-orbit measurements, science data calibration and on-orbit validation. *J Geophys Res Planet* 2011; **116**: E00G19.
25. Pieters C, Shkuratov Y and Kaydash V *et al.* Lunar soil characterization consortium analyses: pyroxene and maturity estimates derived from Clementine image data. *Icarus* 2006; **184**: 83–101.
26. Shkuratov YG, Kaydash VG and Pieters CM. Lunar clinopyroxene and plagioclase: surface distribution and composition. *Sol Syst Res* 2005; **39**: 255–66.
27. Taylor LA, Pieters CM and Keller LP *et al.* Lunar Mare soils: space weathering and the major effects of surface-correlated nanophase Fe. *J Geophys Res Planet* 2001; **106**: 27985–99.
28. Shkuratov YG, Kaydash VG and Starukhina LV *et al.* Lunar surface agglutinates: mapping composition anomalies. *Sol Syst Res* 2007; **41**: 177–85.
29. Hapke B. *Theory of reflectance and emittance spectroscopy*. Cambridge: Cambridge University Press, 2012.
30. Li S and Li L. Radiative transfer modeling for quantifying lunar surface minerals, particle size, and submicroscopic metallic Fe. *J Geophys Res* 2011; **116**: E09001.
31. Li S and Milliken RE. Estimating the modal mineralogy of eucrite and diogenite meteorites using visible-near infrared reflectance spectroscopy. *Meteorit Planet Sci* 2015; **50**: 1821–50.
32. Clegg-Watkins R, Jolliff B and Boyd A *et al.* Photometric characterization of the Chang'e-3 landing site using LROC NAC images. *Icarus* 2016; **273**: 84–95.
33. Clegg RN, Jolliff BL and Robinson MS *et al.* Effects of rocket exhaust on lunar soil reflectance properties. *Icarus* 2014; **227**: 176–94.
34. Hu X, Ma P and Yang Y *et al.* Mineral abundances inferred from in situ reflectance measurements of Chang'E - 4 landing site in South Pole-Aitken basin. *Geophys Res Lett* 2019; **46**: 9439–47.
35. Jolliff BL, Wiczorek MA and Shearer CK *et al.* *New views of the Moon*. Berlin: Walter de Gruyter GmbH & Co KG; 2018.
36. NASA. *Exploring the Moon—A Teacher's Guide with Activities*. <https://www.nasa.gov/pdf/180557main.ETM.Rock.Fact.Sheet.pdf>. 1997.
37. Huang J, Xiao ZY and Flahaut J *et al.* Geological characteristics of Von Karman Crater, Northwestern South Pole-Aitken basin: Chang'E-4 Landing Site Region. *J Geophys Res Planets* 2018; **123**: 1684–700.
38. Qiao L, Ling Z and Fu X *et al.* Geological characterization of the Chang'e-4 landing area on the lunar farside. *Icarus* 2019; **333**: 37–51.
39. Ohtake M, Haruyama J and Matsunaga T *et al.* Performance and scientific objectives of the SELENE (KAGUYA) multiband imager. *Earth Planet Space* 2008; **60**: 257–64.
40. Bickel CE and Warner J. Survey of lunar plutonic and granulitic lithic fragments. In: *Lunar and Planetary Science Conference Proceedings, Houston*, 1978.
41. Warner J and Bickel C. Lunar plutonic rocks: a suite of materials depleted in trace siderophile elements. *Am Mineral* 1978; **63**: 1010–5.
42. Vaughan WM and Head JW. Impact melt differentiation in the South Pole-Aitken basin: some observations and speculations. *Planet Space Sci* 2014; **91**: 101–6.
43. Hurwitz DM and Kring DA. Differentiation of the South Pole-Aitken basin impact melt sheet: implications for lunar exploration. *J Geophys Res Planets* 2014; **119**: 1110–33.

44. Li CL, Liu DW and Liu B *et al.* Chang'E-4 initial spectroscopic identification of lunar far-side mantle-derived materials. *Nature* 2019; **569**: 378–82.
45. Liu B, Li CL and Zhang GL *et al.* Data processing and preliminary results of the Chang'e-3 VIS/NIR imaging spectrometer in-situ analysis. *Res Astron Astrophys* 2014; **14**: 1578–94.
46. Gueymard CA. The sun's total and spectral irradiance for solar energy applications and solar radiation models. *Sol Energy* 2004; **76**: 423–53.
47. Besse S, Sunshine J and Staid M *et al.* A visible and near-infrared photometric correction for moon mineralogy Mapper (M³). *Icarus* 2013; **222**: 229–42.
48. Wu YZ, Besse S and Li JY *et al.* Photometric correction and in-flight calibration of Chang' E-1 Interference Imaging Spectrometer (IIM) data. *Icarus* 2013; **222**: 283–95.
49. Zheng YC, Wang SJ and Ouyang ZY *et al.* CAS-1 lunar soil simulant. *Adv Space Res* 2009; **43**: 448–54.